



Topology optimization of bi-material structures with frequency-domain objectives using time-domain simulation and sensitivity analysis

Pingzhang Zhou^{1,2} · Yingchao Peng³ · Jianbin Du⁴

Received: 17 June 2020 / Revised: 26 November 2020 / Accepted: 4 December 2020 / Published online: 21 January 2021
© The Author(s), under exclusive licence to Springer-Verlag GmbH, DE part of Springer Nature 2021

Abstract

In this paper, we propose to use time-domain transient analysis to compute the response of structures in a wide frequency band by means of Fourier transform. A time-domain adjoint variable method is then developed to carry out the sensitivity analysis of frequency-domain objective functions. By using the concept of frequency response function, it turns out that both the objective function and its sensitivity information at multiple frequencies can be obtained by one original simulation and at most one adjoint simulation, respectively. It is also demonstrated that some commonly used performance indices, e.g., dynamic compliance and input power, are indeed self-adjoint; thus, no extra adjoint simulations are needed, which makes the sensitivity analysis extremely efficient. An obvious distinction between the proposed method and the traditional frequency domain methods is that in our method, the frequency response curves in a wide band can be obtained *in each iteration* with no extra costs. It follows that it is easy to *track* the evolution of the frequency response curve in our method, which is essential in both computational and engineering sense. Several numerical examples are tested to show the effectiveness of the proposed method.

Keywords Topology optimization · Adjoint variable method · Time-domain analysis · Fourier transform · Frequency-domain objectives

1 Introduction

Topology optimization has been known as one of the most challenging and promising methodologies in structural optimization. It has been well studied to find the optimal distribution of materials in the design domain to minimize a specified objective function subject to certain constraints. Until now, more focus is placed on statics-related topology

optimization, while not so much attention has been paid on dynamics-related topology optimization. The dynamic response analysis normally requires more thought about certain obstacles, including the localized modes (Pedersen 2000), the possible non-differentiability of the eigenfrequencies (Seyranian et al. 1994; Du and Olhoff 2007b; Zhou et al. 2017), the higher computational expense (Liu et al. 2012; Yoon 2010), the disjointed design subspaces (Olhoff and Du 2016), etc.

Generally speaking, there are three typical categories of research in the dynamics-related topology optimization:

1. First, the emphasis is placed on the eigenfrequencies of structures. In these papers, either the eigenfrequencies in some fixed order (Seyranian et al. 1994; Zhou et al. 2017; Huang et al. 2010; Zhan et al. 2009; Ma and Kikuchi 1995; Díaz and Kikuchi 1992) or the eigenfrequency gap (Du and Olhoff 2007b; Jensen and Pedersen 2006; Halkjær et al. 2006) is chosen as the objective function.
2. Second, the steady-state frequency response of structures is chosen as the topic. Structural response under the harmonic excitation with fixed frequencies or in

Responsible Editor: YoonYoung Kim

✉ Jianbin Du
dujb@tsinghua.edu.cn

¹ School of Aerospace Engineering, Beijing Institute of Technology, Beijing, People's Republic of China

² School of Vehicle and Mobility, Tsinghua University, Beijing, People's Republic of China

³ Department of Systems Innovation, School of Engineering, The University of Tokyo, Tokyo, Japan

⁴ School of Aerospace Engineering, Tsinghua University, Beijing, People's Republic of China

a frequency range is minimized (Jensen 2007). Normally, the objective functions can be selected as the dynamic compliance (Silva et al. 2019; Zhang and Kang 2016; Ma et al. 1993; Yoon 2010; Niu et al. 2018; Jensen 2007; Olhoff and Du 2008; Venini and Ceresa 2018, 2019), the input power (Jog 2002; Du and Olhoff 2007a; Silva et al. 2020), or the displacement of some specified nodes of interest (Liu et al. 2015; Yoon 2010; Jung et al. 2015; Shu et al. 2011), etc.

3. Third, the transient response of structures when subject to a time-domain excitation is taken into account. Usually the maximum displacement (Zhao and Wang 2017, 2016) in a time range, or the total energy in given elements (Le et al. 2012; Zhao and Wang 2016) is defined as the objective functions to find the optimal topologies.

As stated by Kang et al. (2006) in his review paper, the main themes for time-domain dynamic topology optimization problems can be categorized as three parts, namely the treatment of time-dependent constraints, calculation of design sensitivity, and approximation. In order to improve the efficiency of time-domain topology optimization, Zhao and Wang (2017) propose to use an aggregation functional to transform the original problem formulation into one that is more computational tractable when minimizing the maximum response of the structure over the complete vibration phase in the time-domain. Venini (2016) describes and compares the time-domain and frequency-domain approaches for the minimization of the dynamic compliance of viscoelastic thin beams forced by transient loads. As an approximation method, the equivalent static loads method (Kang et al. 2001; Choi and Park 2002; Park and Kang 2003, 2011) is proposed to solve dynamic response structural optimization problems more efficiently by solving a sequence of related static optimization problems with the same objective and constraint functions as the original problem.

Since the dynamic response analysis normally requires much more computational cost than static analysis, the efficiency of both the simulation and the optimization algorithms is of great importance. Liu et al. (2012) make use of the first and second derivatives of dynamic responses to approximate the dynamic displacement and stress and transform the constrained optimization problems into unconstrained problems by means of interior point penalty function method in the optimization of a plane frame structure. Zhao and Wang (2016) and Liu et al. (2015) investigate two representatives of the model reduction methods, i.e., the mode displacement method and mode acceleration method, for time-domain response problems from the perspective of accuracy and efficiency and compare these two methods with direct integration-based approach. It is found that when the number of time steps

is large the mode acceleration method is superior to the mode displacement method in accuracy and also superior to the direct integration method in efficiency. Also, Yoon (2010) compares some model reduction schemes, e.g., mode superposition, Ritz vector, quasi-static Ritz vector methods from the point of efficiency and accuracy for topology optimization in the frequency domain. Another possibility in reducing the computational burden with structural dynamic response is to use the Padé approximation (Jensen 2007). As commercial software can usually run the computation-intensive finite-element analysis much more efficiently than homemade codes, some researchers try to utilize the professional software as black-boxes to find the FEA solution while implementing the topology optimization algorithms in their homemade codes (Calvel and Mongeau 2007; Jung et al. 2015).

The sensitivity analysis which obtains the derivatives information of responses w.r.t. the design variables is the basis of gradient-based design optimization. Dutta and Ramakrishnan (1998) handle the problem that the design sensitivities for structures under transient dynamic loads are sensitive to the space and time discretization by using an adaptive mesh for a reasonably fine but constant time step. Two discrete approximation methods, namely the differentiate-then-discretize and discretize-then-differentiate approach, are discussed by Jensen et al. (2014). It is showed that (Jensen et al. 2014) inconsistency may exist in the differentiate-then-discretize approach but can be resolved by tuning the time step when solving the motion equation and using more accurate numerical integration formula (e.g., trapezoidal integral formula or Simpson integral formula) in sensitivity analysis procedure. Gu et al. (2000) implement the precise time integration method to find the solution to the motion equation and the sensitivity for linear and nonlinear transient heat conduction and structural transient dynamics problems.

Different objective functions have been used in the dynamic response topology optimization. Jog (2002) proposes two objective functions for the minimization of structural vibration subjected to the periodic loading: (1) the global one, which in this paper is called as the input power, denotes the dissipated power done by the damping force, and has important implications from the viewpoint of noise reduction; (2) the local one considers the vibrations at points of interest. Another commonly used objective function is the dynamic compliance (Olhoff and Du 2016; Silva et al. 2019), which is defined as the inner product of harmonic force amplitude and displacement amplitude in frequency domain. Depending on different perspectives, the dynamic compliance can be interpreted as either a global index (denoting the sum of elemental kinetic energy, potential energy, and dissipated energy) or a local index (denoting the weighted sum of the deformation at loaded region).

It is well known that the dynamic response topology optimization problems are highly nonlinear and may have many disjointed design sub-space, therefore a generalized incremental frequency-domain method is proposed by Olhoff and Du (2016). The basic idea of this method is to conduct the dynamic response topology optimization from different initial excitation frequencies such that different evolutions of the frequency response curve can be performed during the optimization, making it possible to get away from unwanted local optimum with fixed excitation frequency.

To the best knowledge of the authors, in the community of structural topology optimization, there is no research on using time-domain methods in conjunction with frequency-domain objectives. In this paper, we propose to use time-domain transient analysis to find the structural response in a wide frequency band by means of Fourier transform. The superiority of the proposed method is obvious when the frequency band of interest is wide. What's more, the adjoint sensitivity analysis for the frequency-domain objective functions is deduced in detail and the self-adjointness of the dynamic compliance and input power is demonstrated, where the concept of frequency response function plays a key role.

The remaining parts of this paper are arranged as follows. In Section 2, the traditional frequency-domain method is briefly reviewed, after that the time-domain method and the transformation between time domain and frequency domain are introduced. In Section 3, three commonly used performance indices in dynamic response topology optimization are formulated with respect to the frequency band of interest. The topology optimization workflow is described in Section 4. In Section 5, the sensitivity analysis of the objective functions is illustrated, which takes full advantage of the frequency response function. Some numerical examples and discussions are given in Section 6 where the effectiveness and efficiency of the proposed approach are verified. The conclusions are summarized in Section 7. In Appendix, the Newmark method to solve the motion equation is outlined and the approximation of FT via FFT is illustrated.

2 Obtaining structural response in a wide frequency band by time-domain transient analysis

2.1 Traditional frequency-domain method

Let \mathbf{M} , \mathbf{C} , $\mathbf{K} \in \mathbb{R}^{N \times N}$ denote the global mass, damping, and stiffness matrix of the system, and \mathbf{u} , $\mathbf{q} \in \mathbb{R}^N$ denote the global displacement and load vector, here N is the number of dofs in the FEA model, then the motion equation of a

multiple-degrees-of-freedom vibration system driven by a sinusoidal force can be given by:

$$\mathbf{M}\ddot{\mathbf{u}} + \mathbf{C}\dot{\mathbf{u}} + \mathbf{K}\mathbf{u} = \mathbf{q}(t) = \mathbf{Q} \cos(\omega t). \quad (1)$$

Besides (1), appropriate boundary conditions and initial conditions should be set. In this paper, we consider the zero initial condition:

$$\mathbf{u}(t=0) = \mathbf{0}, \quad \dot{\mathbf{u}}(t=0) = \mathbf{0}. \quad (2)$$

In frequency-domain method, it is a common practice to express the harmonic excitation in a complex form:

$$\mathbf{q}(t) = \mathbf{Q} \cos(\omega t) = \text{Re}\{\mathbf{Q}e^{j\omega t}\}. \quad (3)$$

Here, $j = \sqrt{-1}$ is the imaginary unit. Suppose that the *steady-state solution* of (1) can also be expressed as the complex exponential form:

$$\mathbf{u} = \text{Re}\{\mathbf{U}e^{j\omega t}\}, \quad (4)$$

then by substituting (4) into (1) and cancelling out the time-related term $e^{j\omega t}$, we can get the frequency-domain motion equation as:

$$(-\omega^2\mathbf{M} + j\omega\mathbf{C} + \mathbf{K})\mathbf{U} = \mathbf{Q}. \quad (5)$$

Thus, the displacement (in frequency domain) can be expressed as:

$$\mathbf{U} = (-\omega^2\mathbf{M} + j\omega\mathbf{C} + \mathbf{K})^{-1} \mathbf{Q}. \quad (6)$$

Throughout this paper, we use lowercase letters for time-domain vectors, e.g., $\mathbf{u}(t)$, while uppercase letters for the corresponding frequency-domain vectors, e.g., $\mathbf{U}(\omega)$.

2.2 Time-domain method and the transformation between time domain and frequency domain

Now, we seek to directly solve the motion (1) in time domain by time integration methods, such as Newmark method, generalized- α method, etc. The details of these time integration methods are beyond the scope of this paper; the readers are recommended to Zhang et al. (2018) for references. A coarse outline of these methods is given here and a brief summary of the Newmark method is given in the [Appendix](#) section.

Recall that the motion equation is given by:

$$\mathbf{M}\ddot{\mathbf{u}} + \mathbf{C}\dot{\mathbf{u}} + \mathbf{K}\mathbf{u} = \mathbf{q}(t). \quad (7)$$

In time integration methods, in order to find the structural response in a wide frequency band, the excitation $\mathbf{q}(t)$ is chosen judiciously to include the frequency components in the desired frequency band. For simplicity, we consider the following excitation form:

$$\mathbf{q}(t) = \mathbf{q}\mathbf{a} \cdot g(t), \quad (8)$$

where q is the magnitude of the applied load in the loaded region S_q , $\mathbf{a} \in \{0, 1\}^N$ is the spatial distribution pattern while $g(t)$ is the time varying rule. The entries in \mathbf{a} are either 0 (in the unloaded region) or 1 (in the loaded region):

$$a_i = \begin{cases} 1, & i \in S_q, \\ 0, & i \notin S_q, \end{cases} \tag{9}$$

$i = 1, 2, \dots, N$. Both q and \mathbf{a} are constant throughout the optimization procedure. We take $g(t)$ to be the Gauss impulse, and its time domain expression is given by:

$$g(t) = \exp\left[-\frac{(t - t_0)^2}{\sigma^2}\right]. \tag{10}$$

Its spectrum is given by the Fourier transform of (10):

$$\begin{aligned} G(\omega) &= \int_{-\infty}^{\infty} g(t)e^{-j\omega t} dt \\ &= \sigma\sqrt{\pi} \exp\left(-\frac{\sigma^2\omega^2}{4}\right) \exp(-j\omega t_0) \\ &= G_r(\omega) + jG_s(\omega), \end{aligned} \tag{11}$$

where $G_r(\omega)$ and $G_s(\omega)$ are the real and imaginary parts of $G(\omega)$, resp. The highest frequency component in the Gauss impulse is given by:

$$f_{\max} = \frac{\sqrt{2.3}}{\pi\sigma}. \tag{12}$$

In order to make the excitation at $t = 0$ small enough so that no instant shock would act on the structural system at the beginning of simulation (which would introduce unwanted high-frequency components into the system and slow down the convergence of numerical simulations), the time delay parameter may be taken as:

$$t_0 = \sqrt{20}\sigma \approx 4.5\sigma. \tag{13}$$

(13) leads to the initial excitation to be a rather small value:

$$g(t = 0) = e^{-20} \approx 0 \tag{14}$$

In time integration methods, the simulation time $[0, T]$, where T is the final time, is discretized into small time intervals such that a time series can be given:

$$\{0\Delta t, 1\Delta t, \dots, (n - 1)\Delta t\} \tag{15}$$

where Δt is the time increment and n is the total number of sampling points, they are related to T by

$$T = (n - 1)\Delta t. \tag{16}$$

Upon completion, the time integration methods would give the structural response at the discrete time series,

$$u_i(t) = \{u_i(0\Delta t), u_i(1\Delta t), \dots, u_i((n - 1)\Delta t)\} \tag{17}$$

where $u_i(t)$ is the time response at i -th dof. The displacement vector can now be expressed as:

$$\mathbf{u}(t) = \begin{bmatrix} u_1(t) \\ u_2(t) \\ \vdots \\ u_N(t) \end{bmatrix}, \tag{18}$$

Velocity and acceleration can also be obtained at the same time:

$$\dot{\mathbf{u}}(t) = \begin{bmatrix} v_1(t) \\ v_2(t) \\ \vdots \\ v_N(t) \end{bmatrix}, \quad \ddot{\mathbf{u}}(t) = \begin{bmatrix} a_1(t) \\ a_2(t) \\ \vdots \\ a_N(t) \end{bmatrix}. \tag{19}$$

In the [Appendix](#) section, we give a brief review of the Newmark method, which will be used in this paper to find the solution to (7). An important feature of the Newmark method (and indeed all the direct integration methods) is that the triangular decomposition needs to be executed *only once* during a simulation.

Now that the time response is at hand, the frequency response can be derived by means of Fourier transform:

$$\mathbf{U}(\omega) = \begin{bmatrix} U_1(\omega) \\ U_2(\omega) \\ \vdots \\ U_N(\omega) \end{bmatrix}, \tag{20}$$

where

$$\begin{aligned} U_i(\omega) &= \int_0^T u_i(t)e^{-j\omega t} dt \\ &= \int_0^T u_i(t) \cos(\omega t) dt - j \int_0^T u_i(t) \sin(\omega t) dt \\ &= U_{ri}(\omega) + jU_{si}(\omega) \end{aligned} \tag{21}$$

where $i = 1, 2, \dots, N$, $U_{ri}(\omega)$ and $U_{si}(\omega)$ are the real and imaginary parts of $U_i(\omega)$, resp.

Similarly, the spectrum of the excitation can be given by:

$$\mathbf{Q}(\omega) = \begin{bmatrix} Q_1(\omega) \\ Q_2(\omega) \\ \vdots \\ Q_N(\omega) \end{bmatrix} = q\mathbf{a}G(\omega) = q\mathbf{a}[G_r(\omega) + jG_s(\omega)], \tag{22}$$

where $G(\omega)$ has been given in (11).

In practice, the integration in (11) and (21) can be replaced by the discrete Fourier transform (DFT) which has fast algorithms (FFT), c.f. the Appendix section.

3 Performance indices in dynamic response topology optimization

In this section, we briefly review some common performance indices that have been used in dynamic response topology optimization. Since all these indices are defined in the literature for the purpose of single frequency excitation, they will be generalized to be used in occasions where responses in a wide frequency band may be favored.

3.1 Dynamic compliance

Dynamic compliance is a generalization of the static compliance which has been used frequently in the area of structural topology optimization. It is usually defined as:

$$c(\omega) = \left| \mathbf{Q}^\top \mathbf{U}(\omega) \right|. \tag{23}$$

In our case, both \mathbf{Q} and \mathbf{U} can be complex and dependent on frequency, so we use the following definition of dynamic compliance:

$$\begin{aligned} c(\omega) &= \left| \mathbf{Q}^\top(\omega) \mathbf{U}(\omega) \right|, \\ &= \sqrt{T_1^2(\omega) + T_2^2(\omega)}, \end{aligned} \tag{24}$$

where

$$T_1(\omega) = qG_r(\omega)T_3(\omega) - qG_s(\omega)T_4(\omega), \tag{25a}$$

$$T_2(\omega) = qG_r(\omega)T_4(\omega) + qG_s(\omega)T_3(\omega), \tag{25b}$$

$$T_3(\omega) = \sum_{i \in S_q} U_{ri}(\omega), \tag{25c}$$

$$T_4(\omega) = \sum_{i \in S_q} U_{si}(\omega), \tag{25d}$$

C.f. (9), S_q is the set of dofs where loads are applied. G_r and G_s are defined in (11). Since $c(\omega)$ also varies w.r.t. frequency, its integral form would be a proper objective function in our cases:

$$J_1 = \int_{\omega_a}^{\omega_b} c(\omega) d\omega, \tag{26}$$

where $[\omega_a, \omega_b]$ is the frequency band of interest.

3.2 Input power

Input power is defined as the time-averaged power done by the harmonic excitation force:

$$\begin{aligned} p(\omega) &= \frac{1}{T_0} \int_0^{T_0} \mathbf{q}(t) \cdot \mathbf{v}(t) dt \\ &= \frac{1}{T_0} \int_0^{T_0} \text{Re}\{\mathbf{Q}e^{j\omega t}\} \cdot \Re\{\mathbf{V}e^{j\omega t}\} dt \\ &= \frac{1}{T_0} \int_0^{T_0} \text{Re}\{\mathbf{Q}e^{j\omega t}\} \cdot \Re\{j\omega \mathbf{U}e^{j\omega t}\} dt \\ &= \text{Re} \left\{ -\frac{1}{2} j\omega \mathbf{Q}^\top(\omega) \mathbf{U}^*(\omega) \right\} \\ &= -\frac{1}{2} \omega q \sum_{i \in S_q} [G_r(\omega)U_{si}(\omega) - G_s(\omega)U_{ri}(\omega)] \\ &= \frac{1}{2} \omega q G_s(\omega) T_3(\omega) - \frac{1}{2} \omega q G_r(\omega) T_4(\omega) \end{aligned} \tag{27}$$

where

$$T_0 = \frac{2\pi}{\omega} \tag{28}$$

is the period for the harmonic excitation force with angular frequency ω . The symbols G_r and G_s are defined in (11).

It should be noted here that the expression of (27) is more general than the ones that have been used in the literature, but can degenerate into the ones in the literature by setting $G_s(\omega) = 0$. Obviously, one can find that the expression here is more applicable in a general sense.

To consider the input power in a frequency band, we use the following integral form as an objective function:

$$J_2 = \int_{\omega_a}^{\omega_b} p(\omega) d\omega \tag{29}$$

It can be showed that in time-average sense the input power is equal to the dissipated power done by the damping force¹. Thus, by minimizing the input power, the noise radiation can be reduced. So, this index has great importance from the viewpoint of noise control (Jog 2002).

3.3 Displacements at specific locations

Sometimes, it is desired to control the displacements at specific locations: in this case, the performance index can be taken as Yu et al. (2013) and Jensen (2007):

$$\begin{aligned} J_3 &= \int_{\omega_a}^{\omega_b} \left| \mathbf{L}^\top \mathbf{U} \right| d\omega \\ &= \int_{\omega_a}^{\omega_b} \sqrt{(\mathbf{L}^\top \mathbf{U}_r)^2 + (\mathbf{L}^\top \mathbf{U}_s)^2} d\omega, \end{aligned} \tag{30}$$

¹Note that in time-average sense, neither elastic force nor inertial force makes contribution to the active power.

where \mathbf{L} is a vector has 1 in the dofs of interest while 0 elsewhere.

4 Topology optimization workflow

In this section, we briefly review the workflow of density-based topology optimization methods.

In density-based topology optimization methods, the material properties (e.g., Young's modulus E and the mass density ρ) in the i -th element are interpolated using the fictitious density $\tilde{\xi}_i \in [0, 1]$ as:

$$\mathbf{D}_i = \tilde{\xi}_i^p \mathbf{D}_0 + (1 - \tilde{\xi}_i^p) \mathbf{D}_{\min}, \quad (31)$$

$$\rho_i = \tilde{\xi}_i \rho_0 + (1 - \tilde{\xi}_i) \rho_{\min} \quad (32)$$

where $i = 1, 2, \dots, m$; m is the number of elements in the FEA model; \mathbf{D}_0 and ρ_0 are the elasticity matrix and mass density of the stiffer solid material; $\mathbf{D}_{\min} = 0.1\mathbf{D}_0$ and $\rho_{\min} = 0.1\rho_0$ are the elasticity matrix and mass density of the softer base material. Note that we use the bi-material model here.

$\tilde{\xi}_i$ is related to ξ by the filtering procedure:

$$\tilde{\xi}_i = \frac{\sum_{k=1}^m W_{ik} \xi_k}{\sum_{k=1}^m W_{ik}}, \quad (33)$$

and projection procedure (Xu et al. 2010; Wang et al. 2011),

$$\tilde{\xi}_i = \frac{\tanh(\beta_0 \eta) + \tanh(\beta_0 (\tilde{\xi}_i - \eta))}{\tanh(\beta_0 \eta) + \tanh(\beta_0 (1 - \eta))}, \quad (34)$$

where $i = 1, 2, \dots, m$.

In (33), the filter coefficient W_{ik} is defined as

$$W_{ik} = \frac{\bar{W}_{ik}}{\sum_{k=1}^m \bar{W}_{ik}}, \quad (35)$$

$$\bar{W}_{ik} = \max \{r_{\min} - \text{dist}(\Omega_i^e, \Omega_k^e), 0\},$$

$$i, k = 1, 2, \dots, m.$$

In (34), β_0 is a parameter controlling the strength of the projection procedure. During the optimization process, β_0 will gradually increase from 1 to 64, making the final optimized layout crisp and clear. $\eta = 0.5$ is the threshold for the fictitious density. In (35), r_{\min} is a predefined value for filter radius, and $\text{dist}(\Omega_i^e, \Omega_k^e)$ is the Euclidean distance between i -th element and k -th element.

The global stiffness matrix is the assembly of elemental stiffness matrices. In light of (31), the global stiffness matrix can be given by:

$$\mathbf{K} = \sum_{i=1}^m \left[\tilde{\xi}_i^p \mathbf{K}_{i,0} + (1 - \tilde{\xi}_i^p) \mathbf{K}_{i,\min} \right]. \quad (36)$$

where $\mathbf{K}_{i,0}$ and $\mathbf{K}_{i,\min}$ are the stiffness matrices for i -th element ($i = 1, 2, \dots, m$) if it is filled with the stiffer and softer materials, respectively. Both $\mathbf{K}_{i,0}$ and $\mathbf{K}_{i,\min}$ are constant throughout the optimization.

The global mass matrix is the assembly of elemental mass matrices. In light of (32), the global mass matrix \mathbf{M} can be written as:

$$\mathbf{M} = \sum_{i=1}^m \left[\tilde{\xi}_i \mathbf{M}_{i,0} + (1 - \tilde{\xi}_i) \mathbf{M}_{i,\min} \right] \quad (37)$$

where $\mathbf{M}_{i,0}$ and $\mathbf{M}_{i,\min}$ is the elemental mass matrix of i -th element ($i = 1, 2, \dots, m$) if it is filled with the stiffer and softer materials, resp. $\mathbf{M}_{i,0}$ and $\mathbf{M}_{i,\min}$ are constant throughout the optimization.

Notice that the summation symbols in (36) and (37) denote the famous assembly procedure of finite elements, not the algebraic summation.

The commonly used Rayleigh damping model is utilized in this paper to define the damping matrix:

$$\mathbf{C} = \alpha \mathbf{M} + \beta \mathbf{K}. \quad (38)$$

Here, α and β should be carefully determined since they fully control the decay manner of the time-domain response. In this paper, it is assumed that the modal damping ratio ζ is approximately 0.1 in the frequency band [5, 200] Hz considered in the numerical examples of the present paper, so α and β can be given by

$$\begin{bmatrix} \alpha \\ \beta \end{bmatrix} = \frac{2\zeta}{\omega_a + \omega_b} \begin{bmatrix} \omega_a \omega_b \\ 1 \end{bmatrix}. \quad (39)$$

By substituting $\omega_a = 2\pi \cdot 5$ rad/s, $\omega_b = 2\pi \cdot 200$ rad/s, $\zeta = 0.1$ into (39), we can find that

$$\alpha = 6.1299\text{s}^{-1}, \quad \beta = 1.5527 \times 10^{-4} \text{ s} \quad (40)$$

5 Sensitivity analysis

In this section, we carry out the sensitivity analysis of the performance indices introduced in Section 3. The sensitivity analysis is based on adjoint variable method. We will use \mathbf{b} to denote the design variable in this section.

5.1 Sensitivity analysis of a general function

First of all, let us assume a general objective function given by

$$\Psi = \int_0^T \psi(\mathbf{u}, \mathbf{b}, t) dt, \quad (41)$$

where \mathbf{b} is the design variable and should be the fictitious density in topology optimization problems, and \mathbf{u} is the state variable in the motion (7). Both the beginning time $t = 0$ and the final time $t = T$ are fixed throughout the optimization process.

Finding the sensitivity of Ψ w.r.t. the design variable \mathbf{b} under the motion (7) is by no means an easy task. Fortunately,

this hard work has been completed in the literature and we simply cite the result here (Choi and Kim 2005),

$$\frac{\partial \Psi}{\partial b_k} = \int_0^T \left[\frac{\partial^e \psi}{\partial b_k} + \lambda^\top \frac{\partial \mathbf{R}}{\partial b_k} \right] dt, \tag{42}$$

where $\partial^e \psi / \partial b_k$ is the *explicit* partial derivative of ψ w.r.t. b_k , $\lambda(t)$ is the adjoint solution while $\partial \mathbf{R} / \partial b_k$ is given by

$$\frac{\partial \mathbf{R}}{\partial b_k} = \frac{\partial \mathbf{q}}{\partial b_k} - \frac{\partial \mathbf{M}}{\partial b_k} \ddot{\mathbf{u}} - \frac{\partial \mathbf{C}}{\partial b_k} \dot{\mathbf{u}} - \frac{\partial \mathbf{K}}{\partial b_k} \mathbf{u}. \tag{43}$$

One may notice that the term $\partial \mathbf{R} / \partial b_k$ is independent with the objective function Ψ .

For the performance indices used in this paper, i.e., J_1 , J_2 , J_3 , they are not explicitly dependent on the design variable \mathbf{b} . So, the first part in the integral kernel (i.e., $\partial \psi / \partial b_k$) is zero, which can lead to a simpler form of the sensitivity formula:

$$\frac{\partial \Psi}{\partial b_k} = \int_0^T \lambda^\top \frac{\partial \mathbf{R}}{\partial b_k} dt. \tag{44}$$

In addition, in this paper, we do not consider the design-dependent loads, so (43) can be simplified as well:

$$\frac{\partial \mathbf{R}}{\partial b_k} = -\frac{\partial \mathbf{M}}{b_k} \ddot{\mathbf{u}} - \frac{\partial \mathbf{C}}{b_k} \dot{\mathbf{u}} - \frac{\partial \mathbf{K}}{b_k} \mathbf{u}. \tag{45}$$

The differential of the mass matrix, damping matrix, and stiffness matrix over the design variable can be found from the SIMP interpolation scheme (36) and (37).

The adjoint solution $\lambda(t)$ must be found by solving an adjoint ODE given by Choi and Kim (2005):

$$\begin{cases} \hat{\lambda}(\tau = 0) = 0 \\ \hat{\lambda}_{,\tau}(\tau = 0) = 0 \\ \mathbf{M}^\top \hat{\lambda}_{,\tau\tau}(\tau) + \mathbf{C}^\top \hat{\lambda}_{,\tau}(\tau) + \mathbf{K}^\top \hat{\lambda}(\tau) = \frac{\partial \hat{\psi}^\top}{\partial \mathbf{u}}(\mathbf{u}, \mathbf{b}, \tau) \end{cases} \tag{46}$$

Here, $\hat{\lambda}(\tau)$ is the time-reversed version of $\lambda(t)$,

$$\tau(t) = T - t, \quad t(\tau) = T - \tau, \tag{47}$$

so $\lambda(t)$ can be recovered by reversing the time axis again,

$$\lambda(t) = \hat{\lambda}(T - t). \tag{48}$$

$\hat{\lambda}_{,\tau}$ and $\hat{\lambda}_{,\tau\tau}$ are the first and second derivatives of $\hat{\lambda}$ w.r.t. τ , resp. In this paper, we use the hat symbol to identify a variable that is evaluated in the reversed time axis.

Since \mathbf{M} , \mathbf{C} , \mathbf{K} are all symmetric matrices in our case, (46) can be rewritten as:

$$\begin{cases} \hat{\lambda}(\tau = 0) = 0 \\ \hat{\lambda}_{,\tau}(\tau = 0) = 0 \\ \mathbf{M} \hat{\lambda}_{,\tau\tau}(\tau) + \mathbf{C} \hat{\lambda}_{,\tau}(\tau) + \mathbf{K} \hat{\lambda}(\tau) = \frac{\partial \hat{\psi}^\top}{\partial \mathbf{u}}(\mathbf{u}, \mathbf{b}, \tau) \end{cases} \tag{49}$$

By comparing (49) and (7), one can find that the adjoint system is indeed almost the same as the original system, the only difference lies in the right-hand side. So, we can easily find the adjoint solution using the same FEA solver by replacing the excitation $\mathbf{q}(t)$ with the *adjoint excitation*

$$\hat{\mathbf{q}}(\tau) = \frac{\partial \hat{\psi}^\top}{\partial \mathbf{u}}(\mathbf{u}, \mathbf{b}, \tau). \tag{50}$$

We note here that the adjoint excitation is simply the derivative of the integral kernel ψ w.r.t. the state variable \mathbf{u} , but needs to be reversed in the time axis.

5.2 Sensitivity of $U_i(\omega)$

Now, we derive the sensitivity of $U_i(\omega)$, i.e., the displacement spectrum at a specific dof, w.r.t. the design variable \mathbf{b} . This sensitivity information is the basis for the sensitivity of J_1 , J_2 , and J_3 .

As shown beforehand, $U_i(\omega)$ is the Fourier transform of $u_i(t)$:

$$U_i(\omega) = \int_0^T u_i(t) e^{-j\omega t} dt = U_{ri}(\omega) + jU_{si}(\omega), \tag{51}$$

where

$$U_{ri}(\omega) = \int_0^T u_i(t) \cos(\omega t) dt, \tag{52}$$

$$U_{si}(\omega) = -\int_0^T u_i(t) \sin(\omega t) dt,$$

are the real and imaginary parts of U_i , resp. By comparing (51) with (41), one can find that now the integral kernel is

$$\psi = u_i(t) e^{-j\omega t}. \tag{53}$$

By substituting this integral kernel into (50) and keep in mind the time reversing rule (47), we can give the adjoint excitation as

$$\hat{\mathbf{q}}(\tau) = \mathbf{I}_i e^{-j\omega(T-\tau)}, \tag{54}$$

where \mathbf{I}_i is an identity vector that has 1 in i -th entry while 0 elsewhere.

As mentioned many times, the intention of this paper is to efficiently deal with performance indices in a frequency band. But as shown in (54), for each frequency ω , there is a corresponding adjoint excitation $\hat{\mathbf{q}}_i(\tau)$. So it seems that the adjoint simulation should be executed every once for each frequency point of interest, making the sensitivity analysis extremely inefficient. How to resolve this issue? Here, we can take advantage of the linearity nature of the structural system to execute (at most) only one adjoint simulation to find the adjoint solution for all frequency points of interest. Instead of directly using (54) as the adjoint excitation, it is wiser to choose the adjoint excitation as:

$$\tilde{\mathbf{q}}(\tau) = \mathbf{I}_i g(\tau). \tag{55}$$

The difference between (54) and (55) lies in that now we use the Gauss impulse as the time-varying rule, thus the spectrum of both the adjoint excitation and adjoint solution *fully covers the frequency band of interest*. It follows that the sensitivity in the frequency band can be found by (at most) one adjoint simulation.

Let $\tilde{\lambda}(\tau)$ denote the adjoint solution under the excitation $\tilde{q}(\tau)$. Then, the spectrum of them can be given by:

$$\tilde{Q}(\omega) = \mathbf{I}_i G(\omega) \tag{56}$$

$$\tilde{\mathbf{A}} = \begin{bmatrix} \tilde{\Lambda}_1(\omega) \\ \tilde{\Lambda}_2(\omega) \\ \vdots \\ \tilde{\Lambda}_N(\omega) \end{bmatrix} \tag{57}$$

where

$$\tilde{\Lambda}_k(\omega) = \int_0^T \tilde{\lambda}_k(\tau) e^{-j\omega\tau} d\tau \tag{58}$$

is the spectrum of the adjoint solution at k -th dof, and can be found through FFT of $\tilde{\lambda}_k(\tau)$.

Now that the spectra of both the (adjoint) excitation and response are at hand, the frequency response function (FRF) can be given by:

$$H_{ki}(\omega) = \frac{\tilde{\Lambda}_k(\omega)}{G(\omega)} = A_{ki} e^{j\varphi_{ki}}, \quad k = 1, 2, \dots, N \tag{59}$$

where A_{ki} and φ_{ki} are the amplitude and phase of the FRF, resp.

Due to the linearity of the system, now we can directly write out the adjoint solution under the harmonic excitation $\hat{q}_i(\tau)$ by scaling its amplitude with A_{ki} and shifting its phase with φ_{ki} :

$$\hat{\lambda}(\tau) = \begin{Bmatrix} A_{1i} \exp [j(\varphi_{1i} - \omega T + \omega\tau)] \\ A_{2i} \exp [j(\varphi_{2i} - \omega T + \omega\tau)] \\ \vdots \\ A_{Ni} \exp [j(\varphi_{Ni} - \omega T + \omega\tau)] \end{Bmatrix}. \tag{60}$$

By reversing the time axis, the adjoint solution in normal time axis can be given by:

$$\lambda(t) = \begin{Bmatrix} A_{1i} \exp [j(\varphi_{1i} - \omega t)] \\ A_{2i} \exp [j(\varphi_{2i} - \omega t)] \\ \vdots \\ A_{Ni} \exp [j(\varphi_{Ni} - \omega t)] \end{Bmatrix}. \tag{61}$$

Since the adjoint solution is available, now it is straightforward to use (44) to find the sensitivity information, and we repeat it here:

$$\frac{\partial U_i(\omega)}{\partial b_k} = \int_0^T \lambda^\top \frac{\partial \mathbf{R}}{\partial b_k} dt. \tag{62}$$

5.3 Self-adjointness of $T_3(\omega)$ and $T_4(\omega)$

By investigating the expressions for $c(\omega)$ (c.f. (24)) and $p(\omega)$ (c.f. (27)), one may find that the sensitivity of these two terms can be easily obtained with the help of the chain-rule after the sensitivity of $T_3(\omega)$ and $T_4(\omega)$ is resolved. Take $T_3(\omega)$ as an example, now we seek to prove that this term is in fact *self-adjoint*; thus, no additional adjoint simulation is needed to find its sensitivity. We repeat the expression of $T_3(\omega)$ here:

$$\begin{aligned} T_3(\omega) &= \sum_{i \in S_q} U_{ri}(\omega), \\ &= \sum_{i \in S_q} \left[\int_0^T u_i(t) \cos(\omega t) dt \right]. \end{aligned} \tag{63}$$

By comparing (63) with (41), one can find that now the integral kernel is

$$\psi = \sum_{i \in S_q} u_i(t) \cos(\omega t). \tag{64}$$

By using the conclusion in the previous subsection, now we can directly write out the adjoint excitation for $T_3(\omega)$ as

$$\hat{q}_r(\tau) = \mathbf{a} \cos [\omega(T - \tau)] = \mathbf{a} \text{Re} \{ \exp [j\omega(\tau - T)] \}, \tag{65}$$

where \mathbf{a} is the spacial distribution of the loads as defined in (9).

One may find that the excitation (65) is simply the combination of the real parts of (54). What's more, by comparing (65) with (8) it can be found that *the adjoint excitation here has exactly the same distribution with the original excitation*. We have known that the excitation $q(t)$ leads to the structural response $\mathbf{u}(t)$:

$$\begin{aligned} \mathbf{q}(t) = \mathbf{q} \mathbf{a} g(t) &\rightarrow \mathbf{u}(t) = [u_1(t), \dots, u_N(t)]^\top, \\ \mathbf{Q}(\omega) = \mathbf{q} \mathbf{a} G(\omega) &\rightarrow \mathbf{U}(\omega) = [U_1(\omega), \dots, U_N(\omega)]^\top. \end{aligned} \tag{66}$$

So we can now define the FRF from the excitation $\mathbf{q}(t)$ to response $u_i(t)$ as

$$H_i(\omega) = \frac{U_i(\omega)}{qG(\omega)} = A_i e^{j\varphi_i}, \quad i = 1, 2, \dots, N \tag{67}$$

where A_i and φ_i are the amplitude and phase of the FRF, resp.

Thus, the response of the structural system under (65) can be readily given by taking advantage of the linearity of the structural system:

$$\lambda_r(\tau) = \text{Re} \left\{ \exp [j\omega(\tau - T)] A_i e^{j\varphi_i} \right\} = \begin{Bmatrix} A_1 \cos (\varphi_1 + \omega\tau - \omega T) \\ A_2 \cos (\varphi_2 + \omega\tau - \omega T) \\ \vdots \\ A_N \cos (\varphi_N + \omega\tau - \omega T) \end{Bmatrix}. \tag{68}$$

By reversing the time axis, the adjoint solution in normal time axis can be given by:

$$\lambda_r(t) = \begin{Bmatrix} A_1 \cos (\varphi_1 - \omega t) \\ A_2 \cos (\varphi_2 - \omega t) \\ \vdots \\ A_N \cos (\varphi_N - \omega t) \end{Bmatrix}. \tag{69}$$

One may notice that (68) and (69) are simply the combination of the real parts of (60) and (61), resp.

In a similar manner, $T_4(\omega)$ can be rewritten as

$$T_4(\omega) = \sum_{i \in S_q} U_{si}(\omega), = - \sum_{i \in S_q} \left[\int_0^T u_i(t) \sin(\omega t) dt \right]. \tag{70}$$

By comparing (70) with (41), one can find that now the integral kernel is

$$\psi = - \sum_{i \in S_q} u_i(t) \sin(\omega t). \tag{71}$$

The adjoint excitation can be given by

$$\hat{q}_s(\tau) = -\mathbf{a} \sin [\omega(T - \tau)] = \mathbf{a} \text{Im} \{ \exp [j\omega(\tau - T)] \}, \tag{72}$$

which is the combination of the imaginary parts of (54). So the adjoint solution can be given by

$$\lambda_s(t) = \begin{Bmatrix} A_1 \sin (\varphi_1 - \omega t) \\ A_2 \sin (\varphi_2 - \omega t) \\ \vdots \\ A_N \sin (\varphi_N - \omega t) \end{Bmatrix}. \tag{73}$$

One may notice that (73) is simply the combination of the imaginary parts of (61).

After the adjoint solutions are available, the sensitivity of $T_3(\omega)$ and $T_4(\omega)$ can be readily given by

$$\frac{\partial T_3(\omega)}{\partial b_k} = \int_0^T \lambda_r^\top \frac{\partial \mathbf{R}}{\partial b_k} dt, \tag{74a}$$

$$\frac{\partial T_4(\omega)}{\partial b_k} = \int_0^T \lambda_s^\top \frac{\partial \mathbf{R}}{\partial b_k} dt. \tag{74b}$$

5.4 Sensitivity of $c(\omega)$ and J_1

The expression of $c(\omega)$ is given in (24). Since both $\partial T_3/\partial b_k$ and $\partial T_4/\partial b_k$ are available, finding the sensitivity of $c(\omega)$ is now only a matter of chain rule:

$$\frac{\partial c(\omega)}{\partial b_k} = \frac{\partial c}{\partial T_3} \frac{\partial T_3}{\partial b_k} + \frac{\partial c}{\partial T_4} \frac{\partial T_4}{\partial b_k}, \tag{75}$$

where

$$\frac{\partial c}{\partial T_3} = \frac{\partial c}{\partial T_1} \frac{\partial T_1}{\partial T_3} + \frac{\partial c}{\partial T_2} \frac{\partial T_2}{\partial T_3} = \frac{q}{c} (T_1 G_r + T_2 G_s) \tag{76}$$

$$\frac{\partial c}{\partial T_4} = \frac{\partial c}{\partial T_1} \frac{\partial T_1}{\partial T_4} + \frac{\partial c}{\partial T_2} \frac{\partial T_2}{\partial T_4} = \frac{q}{c} (-T_1 G_s + T_2 G_r) \tag{77}$$

Now, the sensitivity of J_1 can be given by:

$$\frac{\partial J_1}{\partial b_k} = \int_{\omega_a}^{\omega_b} \frac{\partial c(\omega)}{\partial b_k} d\omega. \tag{78}$$

The integration here can be evaluated using numerical integration technique.

5.5 Sensitivity of $p(\omega)$ and J_2

The expression of $p(\omega)$ is given in (27). Since both $\partial T_3/\partial b_k$ and $\partial T_4/\partial b_k$ are available, finding the sensitivity of $c(\omega)$ is now only a matter of chain rule:

$$\frac{\partial p(\omega)}{\partial b_k} = \frac{\partial p}{\partial T_3} \frac{\partial T_3}{\partial b_k} + \frac{\partial p}{\partial T_4} \frac{\partial T_4}{\partial b_k}, \tag{79}$$

where

$$\frac{\partial p}{\partial T_3} = \frac{1}{2} q \omega G_s(\omega), \tag{80a}$$

$$\frac{\partial p}{\partial T_4} = -\frac{1}{2} q \omega G_r(\omega). \tag{80b}$$

Now the sensitivity of J_2 can be given by:

$$\frac{\partial J_2}{\partial b_k} = \int_{\omega_a}^{\omega_b} \frac{\partial p(\omega)}{\partial b_k} d\omega. \tag{81}$$

5.6 Sensitivity of J_3

C.f. (30), J_3 is defined as the integration with respect to the frequency band of interest:

$$\begin{aligned}
 J_3 &= \int_{\omega_a}^{\omega_b} |\mathbf{L}^\top \mathbf{U}| \, d\omega \\
 &= \int_{\omega_a}^{\omega_b} \sqrt{(\mathbf{L}^\top \mathbf{U}_r)^2 + (\mathbf{L}^\top \mathbf{U}_s)^2} \, d\omega \\
 &= \int_{\omega_a}^{\omega_b} \sqrt{J_{3r}^2 + J_{3s}^2} \, d\omega
 \end{aligned} \tag{82}$$

where J_{3r} and J_{3s} are

$$J_{3r} = \mathbf{L}^\top \mathbf{U}_r = \sum_{i \in S_l} u_i(t) \cos(\omega t), \tag{83a}$$

$$J_{3s} = \mathbf{L}^\top \mathbf{U}_s = - \sum_{i \in S_l} u_i(t) \sin(\omega t), \tag{83b}$$

where S_l is the set of dofs of interest. By comparing (83) with (41), one can find that now the integral kernel is:

$$\psi_r = \sum_{i \in S_l} u_i(t) \cos(\omega t), \tag{84a}$$

$$\psi_s = - \sum_{i \in S_l} u_i(t) \sin(\omega t). \tag{84b}$$

The adjoint excitations are:

$$\hat{q}_r(\tau) = \mathbf{L} \operatorname{Re} \{ \exp [j\omega(\tau - T)] \}, \tag{85a}$$

$$\hat{q}_s(\tau) = \mathbf{L} \operatorname{Im} \{ \exp [j\omega(\tau - T)] \}. \tag{85b}$$

In practice, we will use the adjoint excitation as

$$\tilde{q}(\tau) = \mathbf{L} g(\tau). \tag{86}$$

Suppose that the adjoint response under $\tilde{q}(\tau)$ is given by $\tilde{\lambda}(\tau)$, then the frequency response function can be given by

$$\mathbf{H}(\omega) = \begin{bmatrix} H_1(\omega) \\ H_1(\omega) \\ \vdots \\ H_N(\omega) \end{bmatrix}, \tag{87}$$

where

$$\begin{aligned}
 H_i(\omega) &= \frac{\tilde{\Lambda}(\omega)}{G(\omega)} = A_i e^{j\varphi_i}, \\
 \tilde{\Lambda}(\omega) &= \int_0^T \tilde{\lambda}_i(\tau) e^{-j\omega\tau} \, d\tau.
 \end{aligned} \tag{88}$$

Thus, the adjoint response under $\hat{q}_r(\tau)$ and $\hat{q}_s(\tau)$ can be given by:

$$\hat{\lambda}_r(\tau) = \begin{Bmatrix} A_1 \cos(\varphi_1 + \omega\tau - \omega T) \\ A_2 \cos(\varphi_2 + \omega\tau - \omega T) \\ \vdots \\ A_N \cos(\varphi_N + \omega\tau - \omega T) \end{Bmatrix}, \tag{89a}$$

$$\hat{\lambda}_s(\tau) = \begin{Bmatrix} A_1 \sin(\varphi_1 + \omega\tau - \omega T) \\ A_2 \sin(\varphi_2 + \omega\tau - \omega T) \\ \vdots \\ A_N \sin(\varphi_N + \omega\tau - \omega T) \end{Bmatrix}. \tag{89b}$$

After time reversing, the adjoint solutions in normal axis are given by:

$$\hat{\lambda}_r(t) = \begin{Bmatrix} A_1 \cos(\varphi_1 - \omega t) \\ A_2 \cos(\varphi_2 - \omega t) \\ \vdots \\ A_N \cos(\varphi_N - \omega t) \end{Bmatrix}, \tag{90a}$$

$$\hat{\lambda}_s(t) = \begin{Bmatrix} A_1 \sin(\varphi_1 - \omega t) \\ A_2 \sin(\varphi_2 - \omega t) \\ \vdots \\ A_N \sin(\varphi_N - \omega t) \end{Bmatrix}. \tag{90b}$$

After the adjoint solutions are available, the sensitivity of $J_{3r}(\omega)$ and $J_{3s}(\omega)$ can be readily given by:

$$\frac{\partial J_{3r}(\omega)}{\partial b_k} = \int_0^T \lambda_r^\top \frac{\partial \mathbf{R}}{\partial b_k} \, dt, \tag{91a}$$

$$\frac{\partial J_{3s}(\omega)}{\partial b_k} = \int_0^T \lambda_s^\top \frac{\partial \mathbf{R}}{\partial b_k} \, dt. \tag{91b}$$

So, finally the sensitivity of J_3 can be given by

$$\frac{\partial J_3}{\partial b_k} = \int_{\omega_a}^{\omega_b} \left[\frac{J_{3r}}{J_3} \frac{\partial J_{3r}(\omega)}{\partial b_k} + \frac{J_{3s}}{J_3} \frac{\partial J_{3s}(\omega)}{\partial b_k} \right] \, d\omega \tag{92}$$

6 Numerical examples

6.1 Bi-material plate under transient pressure loads

In this example, we consider the square plate under transient pressure loads, as shown in Fig. 1. Properties of the stiffer material are $E_0 = 210\text{GPa}$, $\rho_0 = 7830\text{kg/m}^3$, and $\nu = 0.3$. The softer material's properties are $E_{\min} = 0.1E_0$, $\rho_{\min} = 0.1\rho_0$, and $\nu = 0.3$. Geometry parameters are as follows: edge length $\ell = 1 \text{ m}$, load thickness $t = 0.01 \text{ m}$. For amplitude $q = 10\text{N}$ nodes. all Damping parameters α and β are given in (40). The objective is to optimize the plate to minimize the dynamic compliance in a specified frequency

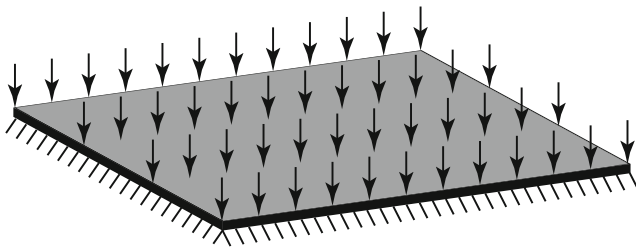


Fig. 1 A bi-material plate. The exterior edges are all fixed. Uniform pressure loads are applied on the upper surface

range, so the mathematical model for this example can be formulated as:

$$\begin{aligned}
 &\text{find} \quad \xi = [\xi_1, \xi_2, \dots, \xi_m]^T \\
 &\text{minimize} \quad J_1 = \int_{\omega_a}^{\omega_b} c(\omega) d\omega \\
 &\text{subject to} \quad \begin{cases} M\ddot{u} + C\dot{u} + Ku = q(t) \\ \sum_{i=1}^m \xi_i V_i \leq \gamma \sum_{i=1}^m V_i \end{cases} \quad (93)
 \end{aligned}$$

where the admissible material usage of the stiffer material is $\gamma = 50\%$, $c(\omega)$ is defined in (24) and (25), $[\omega_a, \omega_b]$ is the predefined excitation frequency band that is kept unchanged during the optimization procedure. The plate is modelled using quadrilateral shell elements. In order to perform a time domain analysis, as discussed in Section 2.2, the Gauss impulse pressure loads with uniform spacial distribution are applied to the plate. The total simulation time is $T = 1$ s, time step $\Delta t = 5 \times 10^{-4}$ s. The plate is discretized into 40×40 shell elements. Newmark method is used to simulate the transient response of the structure.

The $c(\omega)$ curves for the initial design (i.e., the uniform design with each elemental fictitious density equal to the volume fraction $\gamma = 50\%$) are shown as the dotted black line in Fig. 2, from which it can be found that the first resonant frequency² is $f_1 = 55.66$ Hz, and there is only one resonance peak in $[0, 200]$ Hz. Based on this observation, four cases of the frequency range will be considered:

1. $[\omega_a, \omega_b] = [40, 50]$ Hz, i.e., the frequency band of interest is lower than the first resonant frequency.
2. $[\omega_a, \omega_b] = [50, 60]$ Hz, i.e., the frequency band of interest covers the first resonant frequency.
3. $[\omega_a, \omega_b] = [60, 70]$ Hz, i.e., the frequency band of interest is larger than the first resonant frequency.
4. $[\omega_a, \omega_b] = [40, 70]$ Hz. This range is the union of the previous three ranges.

²Note that we use the term *resonant frequency*, rather than *eigenfrequency*, since the resonance frequencies are only a subset of the eigenfrequencies depending on the excitation location and direction.

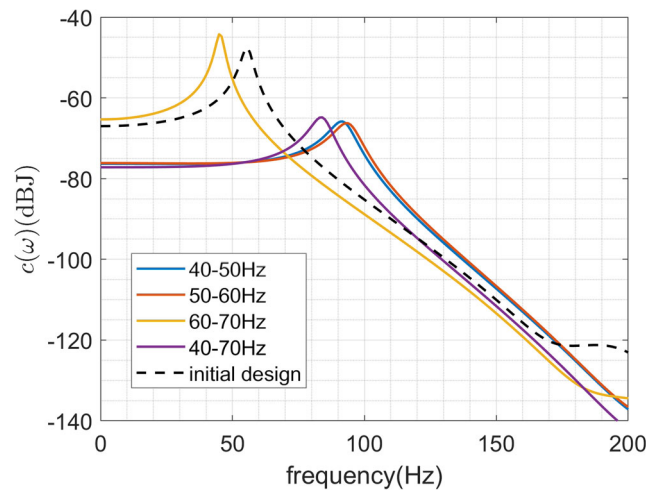


Fig. 2 $c(\omega)$ curve of the initial design and different optimized designs in example 1

Topology optimization results under different frequency range requirements are shown in Figs. 3, 4, 5, and 6, resp.; some key statistics are listed in Table 1, the $c(\omega)$ curves of these final optimized designs are shown in Fig. 2. In the contour plots of the final optimized designs, 0 denotes the softer material while 1 represents the stiffer material. Since the values of $c(\omega)$ would have different magnitudes in different designs, the dB scale is used in Fig. 2 to make these curves easy to identify, i.e.:

$$c(\omega) \text{ [dB]} = 20 \times \lg c(\omega) \text{ [J]} \quad (94)$$

By the way, since we use the time step $\Delta t = 5 \times 10^{-4}$, from the theory of FFT, we can know that the sampling frequency and frequency resolution are:

$$f_s = \frac{1}{\Delta t} = 2000\text{Hz} \gg 200\text{Hz}, \quad (95a)$$

$$\Delta f = \frac{1}{T} = 1\text{Hz}, \quad (95b)$$

resp. From the Nyquist theorem, we know that the $c(\omega)$ curve is trustworthy in the frequency range $[0, 200]$ Hz.

An obvious distinction between our method and the traditional frequency-domain methods is that in our method the frequency response curve far beyond the frequency band of interest can be easily obtained *in each iteration*, which on the contrary is a time-consuming task in frequency-domain methods (where a series of steady-state dynamic analysis is needed). It follows that in our method it is easy to *track* the evolution of the frequency response curve; this feature is important in both computational and engineering sense.

From Fig. 2 (the blue line) and Table 1, we know that the first resonant frequency of the optimized design in Case (1) is $f_1 = 91.80$ Hz, which is significantly greater than that in initial design. This implies that if the frequency band of interest is lower than the first resonant frequency

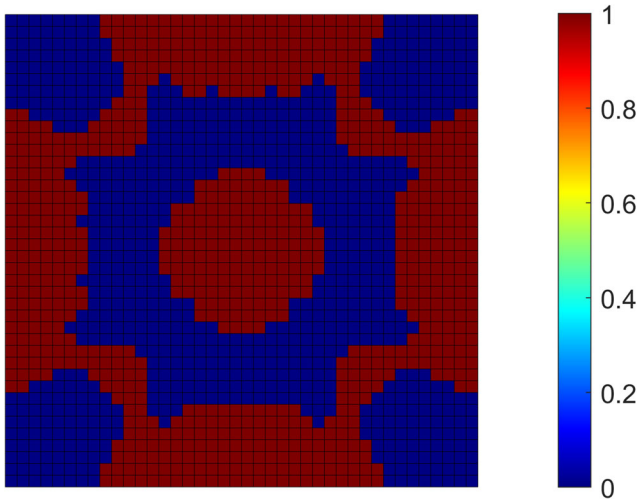


Fig. 3 Topology optimization results of the square plate in example 1 when frequency range is [40, 50] Hz

in the initial design, then by minimizing J_2 we in fact *implicitly* increase the first resonant frequency. The final optimized layout in Fig. 3 shows that the majority of the stiffer material is distributed along the exterior edges where the fixed boundary condition is applied: this is consistent with the higher resonant frequency.

From Fig. 2 (the yellow line) and Table 1, we know that the first resonant frequency of the optimized design in Case (3) is $f_1 = 44.92$ Hz, which is lower than that in initial design. This implies that if the frequency band of interest is higher than the first resonant frequency in the initial design, then by minimizing J_2 we in fact *implicitly* decrease the first resonant frequency. The final optimized layout in Fig. 5 shows that the majority of the stiffer material is distributed in the near-center region which is more prone to

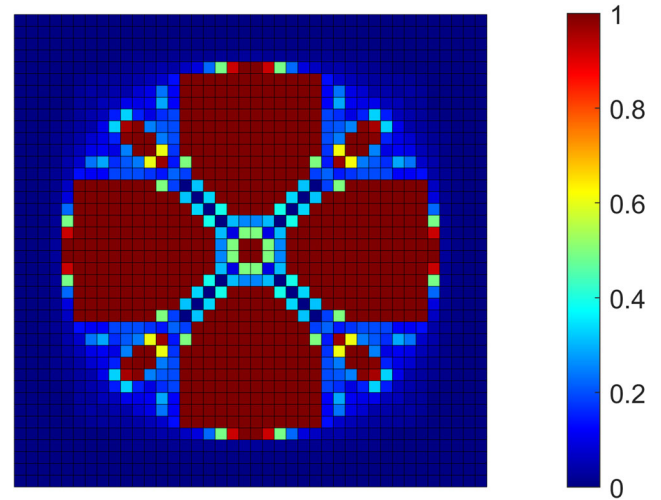


Fig. 5 Topology optimization results of the square plate in example 1 when frequency range is [60, 70] Hz

deformations under the pressure excitation, this is consistent with the lower resonant frequency.

In case (2) and case (4), the frequency band of interest contains the resonant frequency f_1 in the initial design. In these cases, the optimization algorithm would judge between the profits of decreasing and increasing the resonant frequency and make decisions based on which one leads to better performance. From the orange and purple lines in Fig. 2, we know that the resonance frequencies in these two cases are all driven to the right side.

It is interesting to notice that the performance of case (1) is better than that of case (3) in frequency range [60, 70] Hz. In Table 1, $J_1(60 \sim 70 \text{ Hz})$ of case (1) is $1.5344 \times 10^{-3} \text{ J}$, while case (3) is $2.6413 \times 10^{-3} \text{ J}$. This can be explained by the fact that gradient-based numerical

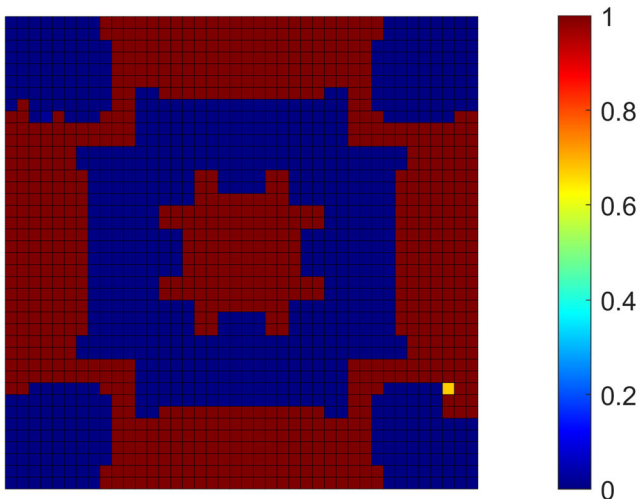


Fig. 4 Topology optimization results of the square plate in example 1 when frequency range is [50, 60] Hz

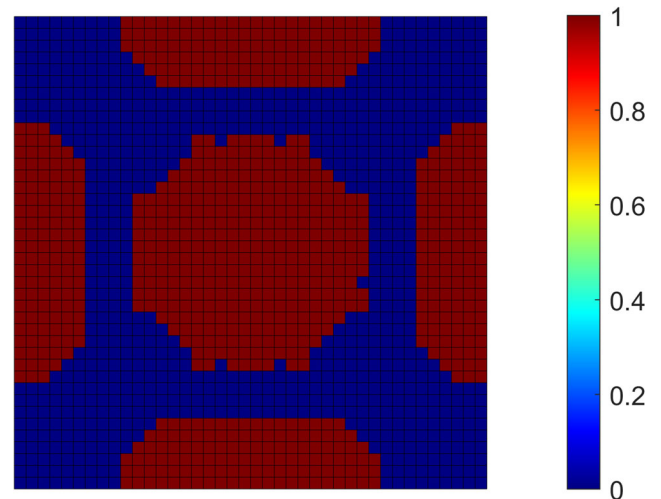


Fig. 6 Topology optimization results of the square plate in example 1 when frequency range is [40, 70] Hz

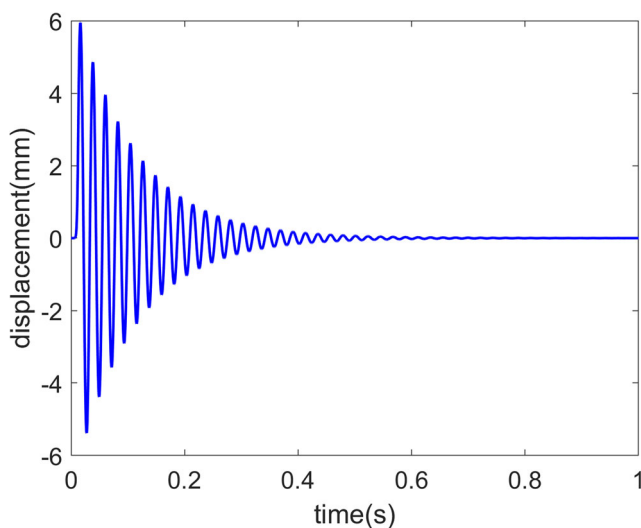
Table 1 Performance of different optimized designs in example 1

Case label	Frequency range (Hz)	f_1 (Hz)	$J_1 (\times 10^{-3} \text{ J})$			
			40~50 Hz	50~60 Hz	60~70 Hz	40~70 Hz
Initial design	-	55.66	10.1657	25.8603	6.7483	45.9423
Case (1)	40~50	91.80	1.5057	1.4074	1.5344	4.7617
Case (2)	50~60	93.75	1.5152	1.4018	1.5022	4.7319
Case (3)	60~70	44.92	35.7247	7.1036	2.6413	47.4743
Case (4)	40~70	83.98	1.4399	1.4136	1.6938	4.8644

optimization algorithms are all greedy and shortsighted and that the dynamic topology optimization problems have many disjointed design subspaces (Olhoff and Du 2016). By looking into Fig. 2, it can be found that driving the resonant frequency to the right direction would make $J_1(60 \sim 70 \text{ Hz})$ become larger in the first stage since the resonance peak would pass by the frequency range. The optimization algorithm thus makes decision that the resonant frequency should be driven to the left, ignoring the fact that driving the resonant frequency to the right side would eventually produce more profits. This phenomenon has been noticed by Olhoff and Du (2016) and the Generalized Incremental Frequency method has been proposed to circumvent this problem.

By comparing the frequency response curves in different cases, it can be found that the larger the first resonant frequency is, the smaller $c(\omega)$ becomes at resonance. This is due to the presence of damping in the FEA model, so the vibration amplitudes would become smaller as the resonant frequency becomes larger.

In order to verify the vibration state of the plate in our simulation, in Fig. 7, we show the time-domain vibration history of the central node in case (3) in the final iteration

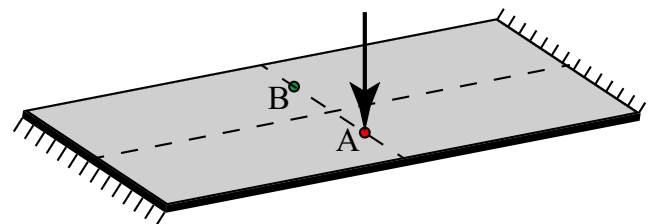
**Fig. 7** Time-domain vibration history of the central node in case (3) of example 1 in the final iteration

as an example. Since the optimized design in case (3) has the smallest value of first-order resonant frequency, it would vibrate more violently than the others. From Fig. 7, one can find that the structure does converge to a nearly static state at the final simulation time $T = 1 \text{ s}$. This indicates that the damping parameters α, β and the simulation time T are all correctly determined. It should be noted here that if these parameters (i.e., α, β, T) are not reasonable, the structure will either still have residual vibration at the end of the simulation, or stop the vibration prematurely. The former will cause the Fourier transform to be inaccurate, and the latter will cause the high-frequency response to be completely suppressed.

It can be found that (cf. Fig. 5) in some final optimized designs not all the design variables converge to $\{0, 1\}$. There are two possible reasons for the “gray” elements in the final optimized design. The first one may be that the optimizing algorithm has not “truly” converged at the end of the iteration since we set the maximum allowable iterations as 100 in all the tested numerical examples. So, the iteration may stop before the design totally converges to $\{0, 1\}$ if the maximum number of iterations is reached. Another possible reason is that in vibration attenuation design, it may be helpful to improve the response characteristics of the structure by setting some soft materials (i.e., “gray” element) in the appropriate positions.

6.2 Rectangular plate under point load

In this example, we consider the rectangular plate under point load, as shown in Fig. 8. Material properties are the

**Fig. 8** Rectangular plate under point load. The left and right edges are fixed. A concentrated load is applied at the 1/4 of the vertical symmetry line (i.e., point A)

same as the previous example. Geometry parameters are as follows: length $\ell = 1$ m, width $w = 0.4$ m, thickness $t = 0.005$ m. Load amplitude $q = 1000$ N. The objective is to optimize the plate to minimize the input power in a specified frequency range, so the mathematical model for this example can be formulated as:

$$\begin{aligned}
 &\text{find} \quad \boldsymbol{\xi} = [\xi_1, \xi_2, \dots, \xi_m]^\top \\
 &\text{minimize} \quad J_2 = \int_{\omega_a}^{\omega_b} p(\omega) d\omega \\
 &\text{subject to} \quad \begin{cases} \mathbf{M}\ddot{\mathbf{u}} + \mathbf{C}\dot{\mathbf{u}} + \mathbf{K}\mathbf{u} = \mathbf{q}(t) \\ \sum_{i=1}^m \tilde{\xi}_i V_i \leq \gamma \sum_{i=1}^m V_i \end{cases} \quad (96)
 \end{aligned}$$

where the admissible material usage of the stiffer material is $\gamma = 50\%$, $p(\omega)$ is defined in (27), $[\omega_a, \omega_b]$ is the predefined excitation frequency band that is kept unchanged during the optimization procedure. The plate is modelled using 50×20 quadrilateral shell elements. Total simulation time is $T = 2$ s; time step $\Delta t = 5 \times 10^{-4}$ s.

In the previous example, there is only one resonance peak in the frequency range $[0, 200]$ Hz. As shown in the black dotted line in Fig. 9, the rectangular plate has four resonance peaks in $[0, 200]$ Hz in the initial design in this example: 17.09Hz, 32.23Hz, 91.8Hz, and 119.1Hz. We consider three cases in this example:

1. $[\omega_a, \omega_b] = [10, 20]$ Hz, i.e., the frequency range of interest contains the first resonant frequency.
2. $[\omega_a, \omega_b] = [20, 80]$ Hz, i.e., the frequency range of interest contains the second resonant frequency.

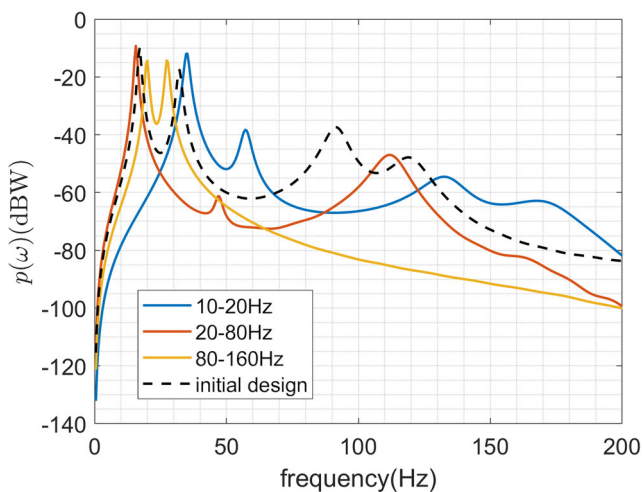


Fig. 9 $p(\omega)$ curve of the initial design and different optimized designs in example 2

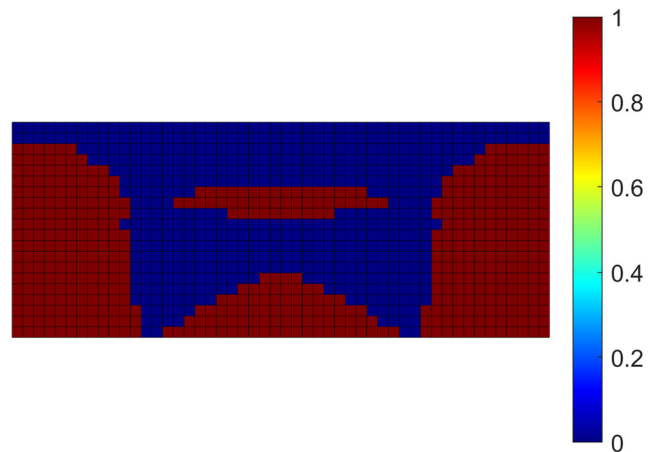


Fig. 10 Topology optimization results of the rectangular plate in example 2 when frequency range is $[10, 20]$ Hz

3. $[\omega_a, \omega_b] = [80, 160]$ Hz, i.e., the frequency range of interest contains the third and fourth resonant frequencies.

The final optimized designs are shown in Figs. 10, 11, and 12, resp., while the $p(\omega)$ curves for these designs are shown in Fig. 9. Some statistics are listed in Table 2. Similar to the previous example, we use the dB scale in Fig. 9:

$$p(\omega) \{dBW\} = 20 \times \lg p(\omega) \{W\}. \quad (97)$$

From Table 2, one can find that each optimized design behaves much better than the rest designs in the frequency range it is optimized. In detail, the J_2 value of case (1) is the best in the frequency range $[10, 20]$ Hz, case (2) is the best in the frequency range $[20, 80]$ Hz, and case (3) is the best in the frequency range $[80, 160]$ Hz. This can also be verified

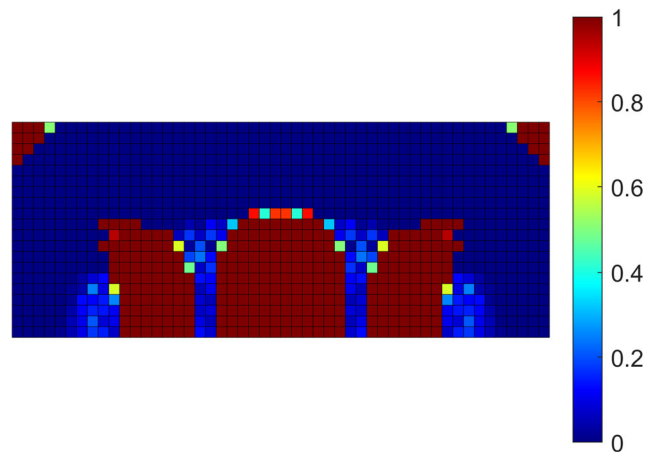


Fig. 11 Topology optimization results of the rectangular plate in example 2 when frequency range is $[20, 80]$ Hz

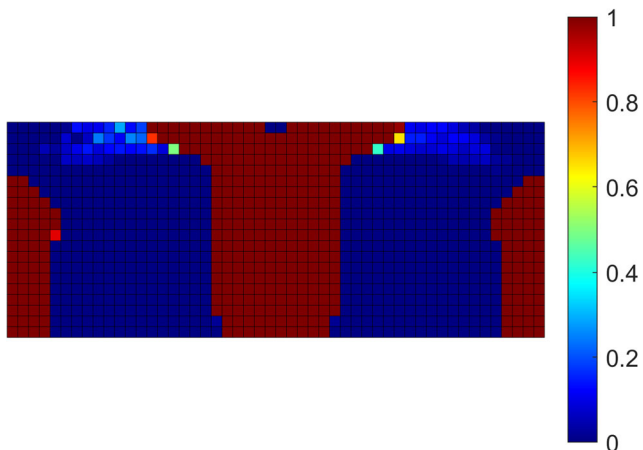


Fig. 12 Topology optimization results of the rectangular plate in example 2 when frequency range is [80, 160] Hz

from Fig. 9. This observation is different from the previous example where only one resonance peak exists.

By looking into Fig. 9, it can be found that in all cases the resonance peaks are either driven out of the frequency range of interest or suppressed into a rather small value. This verifies the ability of our method to tune the structural frequency response in a wide frequency range. Furthermore, because the efficiency of our time-domain optimization method is not influenced by the number of frequencies of interest, it can optimize the structural dynamic response in the whole frequency band of interest in a very efficient manner. The traditional frequency-domain optimization methods, however, are difficult to compromise between the optimization efficiency (which means that the sampling frequency cannot be too high) and the optimization effect (which requires the sampling frequency is sufficiently high).

In Fig. 13, we give the time-domain vibration history of the loaded point in case (2) in the final iteration. From Fig. 13, we know that the structure does converge to a nearly static at the end of simulation $T = 2$ s.

In order to compare the efficiency of the Newmark method with the frequency-domain method, we compare the solution time in each iteration by the Newmark method and the traditional frequency-domain method (i.e., by directly solving the linear system (5)) and list the results in Table 3.

Table 2 Performance of different optimized designs in example 2

Case label	Frequency range(Hz)	J_2 (W)		
		10~20 Hz	20~80 Hz	80~160 Hz
Initial design	-	0.5666	0.4835	0.2402
Case (1)	10~20	0.0034	0.9471	0.0661
Case (2)	20~80	0.6010	0.0478	0.0839
Case (3)	80~160	0.1479	0.7156	0.0043

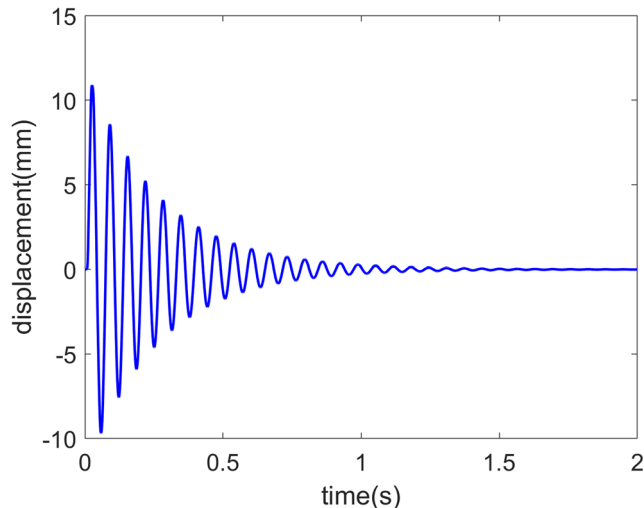


Fig. 13 Time-domain vibration history of the node where concentrated load is applied in case (2) of example 2 in the final iteration

The frequency resolution in both methods is 1 Hz. According to the Nyquist theorem, the dynamic response obtained by Newmark method with $\Delta t = 5 \times 10^{-4}$ s is accurate up to 1000 Hz, so in Table 3 we test four frequency ranges for the case of directly solving (5). Also, two mesh sizes are tested. From Table 3, it can be found that directly solving the linear system (5) is slower than the Newmark method when the frequency range of interest is wide. If the frequency range of interest is narrow, however, direct solving (5) can be faster than the Newmark method. We comment here that our method is by no means limited to the Newmark method as the solver to the motion equation. Other more efficient methods, e.g., the model reduction method, the subspace method, etc., can be freely used as the solver of the motion equation in our method with almost no change in the framework.

6.3 Shell structure under point load with J_3 as the objective function

In this example, we still consider the rectangular plate which is the same as that in Section 6.2, but now we use J_3 as the objective function, i.e., the displacement at Point B as

Table 3 Solution time of motion equation by Newmark method and frequency-domain method

#Mesh	Time (s)				
	Newmark	Directly solving (5)			
		[10, 20] Hz	[20, 80] Hz	[80, 160] Hz	[0, 1000] Hz
50 × 20	1.6627	0.9750	4.9172	6.6173	86.3970
100 × 40	10.4312	4.5129	24.1984	32.0152	414.9453

shown in Fig. 8 is of interest, so the mathematical model for this example can be formulated as:

$$\begin{aligned}
 &\text{find} \quad \xi = [\xi_1, \xi_2, \dots, \xi_m]^T \\
 &\text{minimize} \quad J_3 = \int_{\omega_a}^{\omega_b} |L^T U| d\omega \\
 &\text{subject to} \quad \begin{cases} M\ddot{u} + C\dot{u} + Ku = q(t) \\ \sum_{i=1}^m \tilde{\xi}_i V_i \leq \gamma \sum_{i=1}^m V_i \end{cases} \quad (98)
 \end{aligned}$$

where the admissible material usage of the stiffer material is $\gamma = 50\%$, J_3 is defined in (30), $[\omega_a, \omega_b]$ is the predefined excitation frequency band that is kept unchanged during the optimization procedure, $L \in \{0, 1\}^N$ is a N -dimensional vector whose entries are 1 at the vertical dof of Point B while 0 elsewhere. In this case, the objective function is no longer self-adjoint but the adjoint solution needs to be executed only once. We also consider three cases:

1. $[\omega_a, \omega_b] = [10, 20]$ Hz.
2. $[\omega_a, \omega_b] = [20, 80]$ Hz.
3. $[\omega_a, \omega_b] = [80, 160]$ Hz.

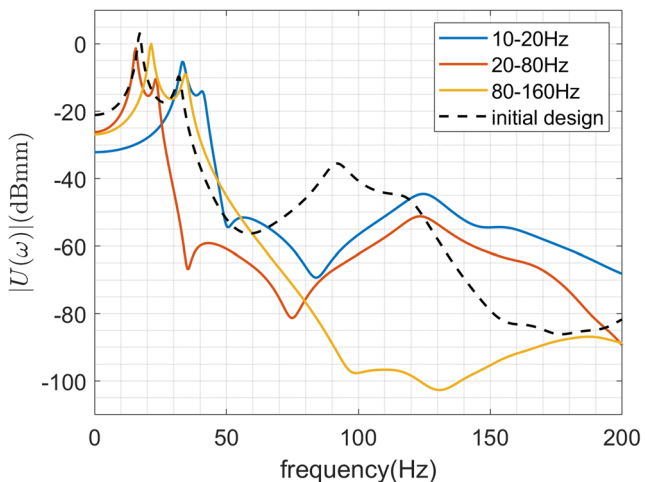


Fig. 14 $|U(\omega)|$ curve of the initial design and different optimized designs in example 3

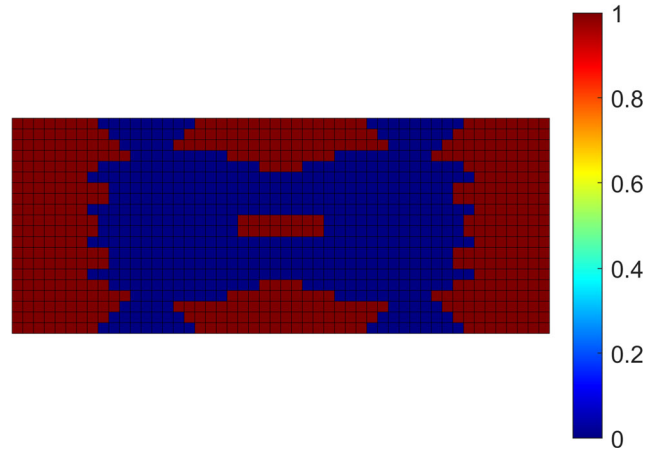


Fig. 15 Topology optimization results of the rectangular plate in example 3 when frequency range is [10, 20] Hz

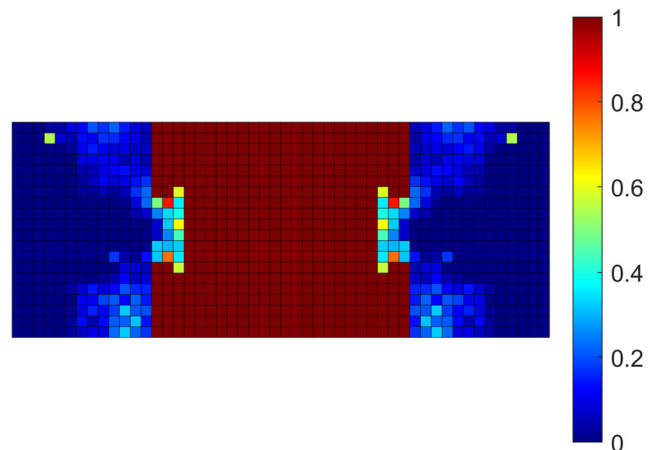


Fig. 16 Topology optimization results of the rectangular plate in example 3 when frequency range is [20, 80] Hz

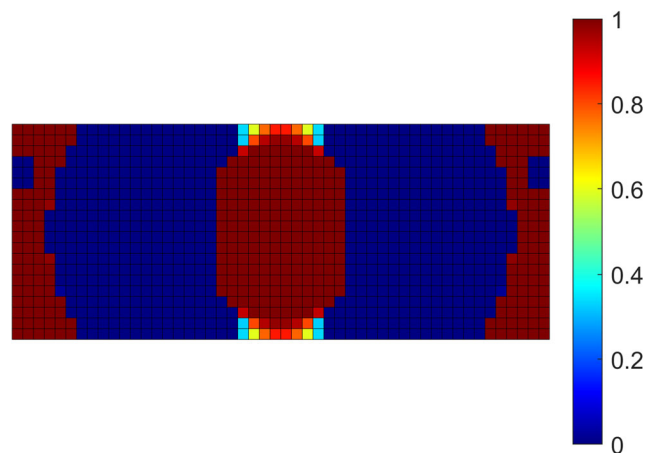


Fig. 17 Topology optimization results of the rectangular plate in example 3 when frequency range is [80, 160] Hz

Table 4 Performance of different optimized designs in example 3

Case label	Frequency range (Hz)	J_3 (mm)		
		10~20 Hz	20~80 Hz	80~160 Hz
Initial design	-	4.7289	3.0496	0.3947
Case (1)	10~20	0.2973	4.1349	0.2021
Case (2)	20~80	2.9384	1.2001	0.0953
Case (3)	80~160	1.2029	5.5552	0.0018

The curve of $U_i(\omega)$, where i corresponds to the z directional dof at point B, for the initial design and different optimized designs is shown in Fig. 14. The final optimized layouts are shown in Figs. 15, 16, and 17, resp. Some statistics are listed in Table 4, from which it can be found that the optimized design always behaves the best among the three cases in the frequency range it is defined. This observation is the same as that in Section 6.2.

Similar to previous examples, we use the dB scale in Fig. 14:

$$U(\omega) \{\text{dBmm}\} = 20 \times \lg U(\omega) \{\text{mm}\}. \quad (99)$$

One may notice that the final layouts in this example are all symmetric about both the horizontal and vertical centerline, while in Section 6.2 the final layouts are only symmetric about the vertical centerline. This is reasonable since in Section 6.2 the concentrated load is applied at point A (c.f. Figure 8) which is not located at the horizontal centerline and the objective considers only the response at this point. In this example, the concentrated load is applied at node A but the response at node B is of interest, making the final optimized designs symmetric about the horizontal centerline as well.

7 Conclusion

A novel time-domain method for the topology optimization of continuum with frequency-domain objectives is proposed, which is especially efficient and preferable when the wide frequency band response is of interest since only one time-domain simulation is enough to find the structural dynamic response throughout the frequency band of interest. The adjoint sensitivity analysis of some commonly used objectives is carried out and it turns out that the dynamic compliance and the input power are all self-adjoint; thus, no extra adjoint simulation is needed, making the sensitivity analysis procedure very efficient.

Through several examples, the effectiveness of our method is demonstrated. According to the numerical results,

different final optimized designs would be generated with different frequency ranges of interest. In engineering practice, the performance of structures is always evaluated in a frequency range, either wide or narrow. So, considering the dynamic performance of structures in a frequency range is important not only in the theoretic sense but also in the engineering practice sense, which is exactly the value of our method.

In this paper, the Newmark method, which is a representative of the direct integration methods, is used to find solutions to the motion equation. But our methods can be freely generalized to be used with other solution methods of the motion equation, e.g., the model reduction method and the subspace method.

Acknowledgments The research is supported by NSFC under Grant Nos. 11902180 and 11772170, China Postdoctoral Science Foundation under Grant Nos. BX20180156 and 2019M650650.

Compliance with ethical standards

Conflict of interest The authors declare that they have no conflict of interest.

Replication of results All the datasets in this study are generated using our homemade codes. The full datasets, as well as the source codes, can be available from the corresponding author with reasonable request.

Appendix

A.1: A brief summary of Newmark method

The Newmark method for the solution of the motion (7) can be outlined as follows. Note that, some symbols, e.g., β , γ , L , have different meaning with the ones used in previous sections.

1. Initialization

- (1) Form the global matrix K , C , M .
- (2) Calculate \ddot{u}_0 with the given initial condition u_0, \dot{u}_0 .

- (3) Using prescribed parameters $\Delta t, \beta, \gamma$ to calculate the integral constants

$$\begin{aligned} c_0 &= \frac{1}{\beta \Delta t^2} & c_1 &= \frac{\gamma}{\beta \Delta t} \\ c_2 &= \frac{1}{\beta \Delta t} & c_3 &= \frac{1}{2\beta} - 1 \\ c_4 &= \frac{\gamma}{\beta} - 1 & c_5 &= \Delta t \left(\frac{\gamma}{2\beta} - 1 \right) \\ c_6 &= \Delta t(1 - \gamma) & c_7 &= \gamma \Delta t \end{aligned}$$

- (a) Form the effective stiffness matrix

$$\hat{\mathbf{K}} = \mathbf{K} + c_0 \mathbf{M} + c_1 \mathbf{C}$$

- (b) Triangular decomposition of $\hat{\mathbf{K}}$

$$\hat{\mathbf{K}} = \mathbf{L} \mathbf{D} \mathbf{L}^T$$

An important observation here is that the triangular decomposition is executed only once in each simulation ahead of the time marching step.

- 2. Time marching: for every time step,

- (1) Compute the effective loads at $t + \Delta t$

$$\hat{\mathbf{q}}_{t+\Delta t} = \mathbf{q}_{t+\Delta t} + \mathbf{M} (c_0 \mathbf{u}_t + c_2 \dot{\mathbf{u}}_t + c_3 \ddot{\mathbf{u}}_t) + \mathbf{C} (c_1 \mathbf{u}_t + c_4 \dot{\mathbf{u}}_t + c_5 \ddot{\mathbf{u}}_t)$$

- (2) Compute the displacement at $t + \Delta t$

$$\mathbf{L} \mathbf{D} \mathbf{L}^T \mathbf{u}_{t+\Delta t} = \hat{\mathbf{q}}_{t+\Delta t}$$

- (3) Compute the acceleration and velocity at $t + \Delta t$

$$\begin{aligned} \ddot{\mathbf{u}}_{t+\Delta t} &= c_0 (\mathbf{u}_{t+\Delta t} - \mathbf{u}_t) - c_2 \dot{\mathbf{u}}_t - c_3 \ddot{\mathbf{q}}_t \\ \dot{\mathbf{u}}_{t+\Delta t} &= \dot{\mathbf{u}}_t + c_6 \ddot{\mathbf{u}}_t + c_7 \ddot{\mathbf{u}}_{t+\Delta t} \end{aligned}$$

A.2: Using FFT to approximate FT

Throughout this paper we use the FT to define the spectrum of a time series signal, i.e.:

$$X(f) = \int_{-\infty}^{+\infty} x(t) e^{-j\omega t} dt \tag{100}$$

The Parseval theorem of the FT indicates that the energy in time domain and frequency domain is equal:

$$\int_{-\infty}^{+\infty} |x(t)|^2 dt = \int_{-\infty}^{+\infty} |X(f)|^2 df \tag{101}$$

If the time series is sampled at discrete time with sampling frequency f_s ,

$$x(t) = \{x_0, x_1, \dots, x_{n-1}\}, \tag{102}$$

then the DFT of this discrete time series is given by

$$X(f) = \{X_0, X_1, \dots, X_{n-1}\}, \tag{103}$$

where

$$X_k = \sum_{n=0}^{N-1} x(n) \exp\left(-j \frac{2\pi}{N} nk\right) \tag{104}$$

The Parseval theorem of the DFT is given by

$$\sum_{k=0}^{n-1} |x_k|^2 = \frac{1}{n} \sum_{k=0}^{n-1} |X_k|^2, \tag{105}$$

which can be rewritten as

$$\sum_{k=0}^{n-1} |x_k|^2 dt = \sum_{k=0}^{n-1} |dt \cdot X_k|^2 df \tag{106}$$

By comparing (106) and (101), we can find that in order to use DFT to approximate FT, the spectrum obtained by DFT should be scaled:

$$X_k^{sc} = X_k \cdot dt. \tag{107}$$

We apply this scale in all the numerical examples. In MATLAB, this procedure can be easily done by the following codes:

$$\mathbf{X} = \text{fft}(\mathbf{x}) * dt; \tag{108}$$

The sampling frequency f_s , the sampling interval Δt , and the frequency resolution Δf are related by:

$$f_s = \frac{1}{\Delta t}, \quad \Delta f = \frac{f_s}{n} \tag{109}$$

References

Calvel S, Mongeau M (2007) Black-box structural optimization of a mechanical component. *Comput Ind Eng* 53(3):514–530. <https://doi.org/10.1016/j.cie.2007.05.009>

Choi WS, Park GJ (2002) Structural optimization using equivalent static loads at all time intervals. *Comput Methods Appl Mech Eng* 191(19):2105–2122. [https://doi.org/10.1016/S0045-7825\(01\)00373-5](https://doi.org/10.1016/S0045-7825(01)00373-5)

Choi KK, Kim NH (2005) *Structural Sensitivity Analysis and Optimization 1: Linear Systems*. Springer, New York

Díaz AR, Kikuchi N (1992) Solutions to shape and topology eigenvalue optimization problems using a homogenization method. *Int J Numer Methods Eng* 35(7):1487–1502

Du J, Olhoff N (2007a) Minimization of sound radiation from vibrating bi-material structures using topology optimization. *Struct Multidiscip Optim* 33(4-5):305–321. <https://doi.org/10.1007/s00158-006-0088-9>

Du J, Olhoff N (2007b) Topological design of freely vibrating continuum structures for maximum values of simple and multiple eigenfrequencies and frequency gaps. *Struct Multidiscip Optim* 34(2):91–110. <https://doi.org/10.1007/s00158-007-0101-y>

Dutta A, Ramakrishnan C (1998) Accurate computation of design sensitivities for structures under transient dynamic loads using time marching scheme. *Int J Numer Methods Eng* 41(6):977–999

Gu Y, Chen B, Zhang H, Liu S (2000) Structural Optimization for Transient Response Constraints with Software JIFEX. *J Appl Sci Eng* 3(3):173–186

Halkjær S, Sigmund O, Jensen JS (2006) Maximizing band gaps in plate structures. *Struct Multidiscip Optim* 32(4):263–275

- Huang X, Zuo ZH, Xie YM (2010) Evolutionary topological optimization of vibrating continuum structures for natural frequencies. *Comput Struct* 88(5):357–364
- Jensen JS (2007) Topology optimization of dynamics problems with padé approximants. *Int J Numer Methods Eng* 72(13):1605–1630. <https://doi.org/10.1002/nme.2065>
- Jensen JS, Pedersen NL (2006) On maximal eigenfrequency separation in two-material structures: the 1d and 2d scalar cases. *J Sound Vibr* 289(4):967–986
- Jensen JS, Nakshatrala PB, Tortorelli DA (2014) On the consistency of adjoint sensitivity analysis for structural optimization of linear dynamic problems. *Struct Multidiscip Optim* pp 831–837. <https://doi.org/10.1007/s00158-013-1024-4>
- Jog C (2002) Topology design of structures subjected to periodic loading. *J Sound Vibr* 253(3):687–709
- Jung J, Hyun J, Goo S, Wang S (2015) An efficient design sensitivity analysis using element energies for topology optimization of a frequency response problem. *Comput Methods Appl Mech Eng* 296:196–210. <https://doi.org/10.1016/j.cma.2015.06.019>
- Kang BS, Choi WS, Park GJ (2001) Structural optimization under equivalent static loads transformed from dynamic loads based on displacement. *Comput Struct* 79(2):145–154. [https://doi.org/10.1016/S0045-7949\(00\)00127-9](https://doi.org/10.1016/S0045-7949(00)00127-9)
- Kang BS, Park GJ, Arora JS (2006) A review of optimization of structures subjected to transient loads. *Struct Multidiscip Optim* 31(2):81–95. <https://doi.org/10.1007/s00158-005-0575-4>
- Le C, Bruns TE, Tortorelli DA (2012) Material microstructure optimization for linear elastodynamic energy wave management. *J Mech Phys Solids* 60(2):351–378. <https://doi.org/10.1016/j.jmps.2011.09.002>
- Liu Q, Zhang J, Yan L (2012) Optimization design of structures subjected to transient loads using first and second derivatives of dynamic displacement and stress. *Shock Vibr* 19:1445–1461. <https://doi.org/10.3233/SAV-2012-0685>
- Liu H, Zhang W, Gao T (2015) A comparative study of dynamic analysis methods for structural topology optimization under harmonic force excitations. *Struct Multidiscip Optim* 51(6):1321–1333. <https://doi.org/10.1007/s00158-014-1218-4>
- Ma ZD, Kikuchi N, Hagiwara I (1993) Structural topology and shape optimization for a frequency response problem. *Comput Mech* 13(3):157–174
- Ma ZD, Kikuchi N (1995) Topological design for vibrating structures. *Comput Methods Appl Mech Eng* 121(1):259–280
- Niu B, He X, Shan Y, Yang R (2018) On objective functions of minimizing the vibration response of continuum structures subjected to external harmonic excitation. *Struct Multidiscip Optim* 57(6):2291–2307. <https://doi.org/10.1007/s00158-017-1859-1>
- Olhoff N, Du J (2008) On topological design optimization of structures against vibration and noise emission. In: *Computational Aspects of Structural Acoustics and Vibration*, pp 217–276
- Olhoff N, Du J (2016) Generalized incremental frequency method for topological design of continuum structures for minimum dynamic compliance subject to forced vibration at a prescribed low or high value of the excitation frequency. *Struct Multidiscip Optim* 54(5):1113–1141. <https://doi.org/10.1007/s00158-016-1574-3>
- Park GJ, Kang BS (2003) Validation of a structural optimization algorithm transforming dynamic loads into equivalent static loads. *J Optim Theory Appl* 118(1):191–200. <https://doi.org/10.1023/A:1024799727258>
- Park GJ (2011) Technical overview of the equivalent static loads method for non-linear static response structural optimization. *Struct Multidiscip Optim* 43(3):319–337. <https://doi.org/10.1007/s00158-010-0530-x>
- Pedersen NL (2000) Maximization of eigenvalues using topology optimization. *Struct Multidiscip Optim* 20(1):2–11
- Seyranian AP, Lund E, Oloff N (1994) Multiple eigenvalues in structural optimization problems. *Struct Optim* 8(4):207–227
- Shu L, Yu M, Fang Z, Ma Z, Wei P (2011) Level set based structural topology optimization for minimizing frequency response. *J Sound Vibr* 330(24):5820–5834. <https://doi.org/10.1016/j.jsv.2011.07.026>
- Silva OM, Neves MM, Lenzi A (2019) A critical analysis of using the dynamic compliance as objective function in topology optimization of one-material structures considering steady-state forced vibration problems. *J Sound Vibr* 444:1–20. <https://doi.org/10.1016/j.jsv.2018.12.030>
- Silva OM, Neves MM, Lenzi A (2020) On the use of active and reactive input power in topology optimization of one-material structures considering steady-state forced vibration problems. *J Sound Vibr* 464:114989. <https://doi.org/10.1016/j.jsv.2019.114989>
- Venini P (2016) Dynamic compliance optimization : Time vs frequency domain strategies. *Comput Struct* 177:12–22. <https://doi.org/10.1016/j.compstruc.2016.07.012>
- Venini P, Ceresa P (2018) A rational h_∞ -norm-based approach for the optimal design of seismically excited reinforced concrete frames. *Earthquake Eng Struct Dyn* 47(6):1522–1543. <https://doi.org/10.1002/eqe.3028>
- Venini P (2019) Topology optimization of dynamic systems under uncertain loads: An h_∞ -norm-based approach. *J Comput Nonlinear Dyn* 14:021007–1–021007–9
- Wang F, Lazarov BS, Sigmund O (2011) On projection methods, convergence and robust formulations in topology optimization. *Struct Multidiscip Optim* 43(6):767–784
- Xu S, Cai Y, Cheng G (2010) Volume preserving nonlinear density filter based on heaviside functions. *Struct Multidiscip Optim* 41(4):495–505
- Yoon GH (2010) Structural topology optimization for frequency response problem using model reduction schemes. *Comput Methods Appl Mech Eng* 199(25):1744–1763
- Yu Y, Gwon I, Byung J, Kwak M (2013) Topology optimization for a frequency response and its application to a violin bridge. *Struct Multidiscip Optim* 48(3):627–636. <https://doi.org/10.1007/s00158-013-0907-8>
- Zhan J, Zhang X, Hu J (2009) Maximization of values of simple and multiple eigenfrequencies of continuum structures using topology optimization. In: *2009 International Conference on Measuring Technology and Mechatronics Automation*, vol 2, pp 833–837. <https://doi.org/10.1109/ICMTMA.2009.497>
- Zhang X, Kang Z (2016) Robust topology optimization for dynamic compliance minimization under uncertain harmonic excitations with inhomogeneous eigenvalue analysis. *Struct Multidiscip Optim* 54(6):1469–1484. <https://doi.org/10.1007/s00158-016-1607-y>
- Zhang X, Wang T, Liu Y (2018) *Computational dynamics*, 2nd edn. Tsinghua University Press, Beijing
- Zhao J, Wang C (2016) Dynamic response topology optimization in the time domain using model reduction method. *Struct Multidiscip Optim* 53(1):101–114. <https://doi.org/10.1007/s00158-015-1328-7>
- Zhao J, Wang C (2017) Topology optimization for minimizing the maximum dynamic response in the time domain using aggregation functional method. *Comput Struct* 190:41–60. <https://doi.org/10.1016/j.compstruc.2017.05.002>
- Zhou P, Du J, Lü Z (2017) Topology optimization of freely vibrating continuum structures based on nonsmooth optimization. *Struct Multidiscip Optim* 56(3):603–618. <https://doi.org/10.1007/s00158-017-1677-5>

Publisher's note Springer Nature remains neutral with regard to jurisdictional claims in published maps and institutional affiliations.